Materials Characterization 185 (2022) 111722

Contents lists available at ScienceDirect

Materials Characterization

journal homepage: www.elsevier.com/locate/matchar

Microstructure evolution, mechanical properties and corrosion behavior of biodegradable Zn-2Cu-0.8Li alloy during room temperature drawing

Zhiqiang Gao [a], Xiyuan Zhang [a], Hua Huang [a], Chun Chen [a], Jimiao Jiang [a], Jialin Niu [a,*], Matthew Dargusch [b], Guangyin Yuan [a,*]

[a] National Engineering Research Center of Light Alloy Net Forming and Key State Laboratory of Metal Matrix Composites, Shanghai Jiao Tong University, Shanghai 200240, China

[b] School of Mechanical and Mining Engineering, The University of Queensland St Lucia Qld 4072, Australia

ARTICLE INFO

Keywords:
Biodegradable Zn-alloys
Cold drawing
Microstructures
Mechanical properties
Natural aging

ABSTRACT

Biodegradable Zn-based alloys exhibit promising application prospects due to their suitable degradation rates and acceptable biocompatibility. However, unstable mechanical properties during room-temperature storage limit their application potential. In this study, Zn-2Cu-0.8Li (wt%) alloy wires with excellent and stable mechanical properties were prepared by hot extrusion followed by multi-pass cold drawing. For the as-extruded Zn-2Cu-0.8Li alloy of a $[\bar{1}2\bar{1}0]//ED$ texture, (Li, Cu)Zn_4 phase (volume fraction: 84.4 ± 2.4%) is found to be the matrix, and the remaining phase is Zn-based solid solution (η-Zn phase). During cold drawing, the (Li, Cu)Zn_4 phase was continuously elongated, and its original texture gradually evolved into intensive $[01\bar{1}0]//DD$ fiber texture. In contrast, the η-Zn phase exhibits an evidently refined grain structure and weakened texture due to dynamic recrystallization (DRX). Accordingly, the ultimate tensile strength was significantly improved from348.1 ± 3.1 MPa (as-extruded rod: Ø 6 mm) to 450.3 ± 8.7 MPa (as-drawn wire: Ø 3 mm), with the elongation decreasing from 37.1 ± 2.1% to 29.5 ± 1.3%. After 6-month natural aging, the as-drawn wire showed desirable mechanical stability, with basically unchanged mechanical properties. The corrosion rate of as-drawn wire with a diameter of 3 mm in c-SBF solution exhibits a 46% increase (from 212.07 ± 10.73 μm/year to 309.81 ± 16.53 μm/year) after cold drawing. Given the excellent mechanical properties and suitable corrosion rate, the Zn-2Cu-0.8Li wires are proposed as a promising material for biodegradable implants.

1. Introduction

Biodegradable metals including Fe-based alloys, Mg-based alloys and Zn-based alloys have attracted increasing attention in the past two decades, because not only do these alloys possess good mechanical and processing properties as metallic materials, but they also are absorbable in the human body [1–3]. Among them, Zn alloys exhibit suitable degradation rates that are usually lower than the rates observed for Mg-based alloys but higher than those of Fe-based alloys, along with promising application prospects for application in various biodegradable implant devices. However, the mechanical properties of pure Zn [4] are far from the critical benchmarks for clinical applications like vascular stents requiring the ultimate strength of more than 300 MPa and elongation of more than 20% [5]. To improve the comprehensive mechanical properties of Zn alloys, alloying is an efficient strategy. Many new medical zinc alloys have been developed by alloying with a wide range of elements including Cu [6,7], Mn [8,9], Ag [10,11], Fe [12,13], Li [14,15], Mg [16,17], Ca [18], Sr [19]. A Zn-0.8Li-0.4 Mg alloy has the highest strength of about 650 MPa that has ever been reported in biodegradable Zn alloys [20]. However, such high strength is acquired by significantly sacrificing the plasticity which results in a low elongation of about 3%. Wtroba et al. [21] fabricated an as-rolled Zn-3Ag-0.5 Mg alloy which exhibited excellent ductility with about 200% elongation but an insufficient ultimate strength lower than 230 MPa. However, the ideal medical biodegradable alloys need both high strength and enough ductility. Moreover, another challenge in Zn alloys is natural aging caused by phase transformations occurring below or at room temperature. For instance, after storage at room temperature for three months, the elongation of Zn-Mg alloy decreased from 34% to 3%, accompanied by a sharp increase in mechanical strength due to the lower stability of microstructure and the precipitation of hard Mg_2Zn_{11} phases in grain boundaries [22]. The natural aging appearing in Zn-

* Corresponding authors.
E-mail addresses: niujialin@sjtu.edu.cn (J. Niu), gyyuan@sjtu.edu.cn (G. Yuan).

https://doi.org/10.1016/j.matchar.2022.111722
Received 14 November 2021; Received in revised form 22 December 2021; Accepted 4 January 2022
Available online 7 January 2022

based clinical materials would make it difficult to maintain the mechanical stability in the treatment period, resulting in early failure.

Aiming to solve the natural aging problem, our group has developed a Zn-Cu binary alloy, with a strength lower than 300 MPa and elongation of about 50% [23]. The mechanical properties of the Zn-Cu alloy were almost unchanged during 20 months of storage at room temperature, showing excellent thermostability and anti-aging property [24]. Meanwhile, in vitro and in vivo experiments have demonstrated that Zn-xCu ($x < 4$ wt%) alloys have good biocompatibility and antibacterial ability [25,26]. In addition, by adding the third component, their mechanical properties could be further improved [27–29]. According to our previous work using first principle calculations, Li is one of the most efficient alloying elements for Zn alloys strengthening [30]. Furthermore, the Li element has good biocompatibility in a low concentration according to the previous studies [31]. Zhao et al. [32] fabricated the as-rolled Zn-xLi alloy and found that with the increase of Li content, the strength of the alloy was significantly increased. When the content of Li was more than 0.6% wt%, the tensile strength of alloy could easily exceed 450 MPa, but the elongation was less than 2%. Therefore, in this work we further added Li element to some proper extent into Zn-Cu alloy and developed a novel Zn-Cu-Li ternary alloy with high strength and ductility

On the other hand, biodegradable zinc alloys need to be processed into various profiles before final fabrication into different implants. Wires are one kind of important raw material, which could be used in small screws, anastomotic nails, braided scaffolds [33,34], etc. During the preparation of wires, Zn alloys would usually experience large deformation through multi-pass drawing, and their mechanical properties could also be regulated by adjusting the microstructures of the alloys. Moreover, Zn-based alloys usually have excellent deformation ability at relatively low temperatures due to their low melting temperature and activating of dynamic recrystallization, which is conducive to the production of Zn-based wires. Wang et al. [35] prepared Zn-0.02wt %Mg wires (0.8 mm in diameter) with a tensile strength of 455 MPa through a multi-pass drawing, but the elongation was only 5.4%. Mostaed et al. [36] fabricated Zn-Ag-Mn ultrafine wires, which exhibited high ductility with an elongation of more than 200%, but the mechanical strength was only 130 MPa. Therefore, further studies are necessary on the drawing process and microstructure regulation to improve the mechanical properties of Zn alloy wires.

In this work, the newly developed Zn-2Cu-0.8Li ternary alloy with high strength and ductility was processed into wires through mulita-pass cold drawing. The microstructure evolution during the drawing, as well as its effect on mechanical properties and corrosion behavior were discussed.

2. Material and methods

2.1. Materials fabrication and processing

The Zn-2Cu-0.8Li alloy (wt%) was prepared by gravity casting using commercially pure Zn (99.99%), pure Cu (99.99%) and pure Li (99.999%). The pure Zn ingot, Cu sheet and Li particles were successively melted in a graphite crucible. When the Li particles were added, a mixed protective gas of CO_2 and SF_6 was used to isolate the air and prevent the burning loss of lithium. After fully melting and standing for 10 min, the melt was poured into a cold mold for solidification. The chemical compositions of Zn-2Cu-0.8Li alloy were measured through an inductively coupled plasma atomic emission spectrometer (ICP-AES). The results have shown that the content of Cu and Li was 1.93 wt% and 0.75 wt%, respectively. After homogenization at 350°C for 24 h, the as-cast ingot was extruded at 300°C with an extrusion ratio of 100, and the extruded rod with a diameter of 6 mm was obtained. Then, the extruded rod underwent multiple passes cold drawing along the extrusion direction and was finally processed into Zn alloy wires with a diameter of 3 mm. The amount of deformation during each drawing pass was about 7%, and the speed was about 10 m/min. The deformation was measured through area reduction (AR) of the cross-section according to equation (1):

$$AR = \left(\left(D_0^2 - D_f^2\right)\Big/ D_0^2\right) \times 100\% \quad (1)$$

Where the D_0 and D_f represent the initial diameter of extruded rod and final diameter of drawn wire, respectively. The wires with a diameter of 5 mm (30.6% AR), 4 mm (55.6% AR) and 3 mm (75%AR) were chosen for the this study.

2.2. Microstructure characterization

The phase composition of as-cast, as-extruded and as-drawn samples were analyzed through X-ray diffraction (XRD, Rigaku, Japan) with Cu Kα radiation where the scanning speed was 5°/min and 2θ was from 20° to 90°. The samples for microstructure analysis were ground through 320#, 1200#, 3000# and 7000# emery paper and then polished by 0.5 μm diamond paste, and subsequently etched by a Cr_2O_3-Na_2SO_4 mixed aqueous solution. These samples were observed using an optical microscope (OM, Zeiss Axio Observer A1, Germany) and scanning electron microscope (SEM, Nova230, FEI, America) with energy dispersive spectrometry (EDS). Because Li element cannot be detected by EDS, the ultra-high resolution scanning electron microscope-focused ion beam time of flight secondary ion mass spectrometry (TOFSIMS, GAIA3 GMU Model, Czech Republic) was used to detect the distribution of Li. The texture of the as-extruded and as-drawn samples and the volume fraction and grain size of different phases were measured through electron backscattering diffraction (EBSD). The phase structure parameters and morphology of the secondary phase of as-drawn wire were identified further using transmission electron microscope (TEM, 2100F, JEOL, Japan). The samples for TEM observation were cut into disks from the cross-section of the as-drawn wires. After the disks were ground to a thickness of 40 μm, they were firstly thinned through an automatic twin-jet electro-polisher in a perchloric acid alcohol solution at 55 V and −40°C, and then experienced the final ion beam thinning by Gatan Precision Ion Polishing System for 30 min at −160°C.

2.3. Tensile test

The standard cylindrical samples for tensile testing were cut from the as-extruded rod and as-drawn wires with a length of 60 mm and a gauge length of 20 mm according to the ASTM E8-16a [37]. Three parallel samples were conducted to ensure the accuracy of the tensile test. The mechanical properties were measured by a universal material testing machine (Zwick/Roell Z20, Germany) with an extension rate of 1×10^{-3} s^{-1}. The tensile direction was parallel to the drawing (extrusion) direction. In addition, the tensile mechanical properties of the as-drawn wires after storage at room temperature for 6 months were also tested to evaluate the thermostability.

2.4. Corrosion measurement

2.4.1. Immersion test

The samples for immersion tests were cut into cylinders with a length of 20 mm. The surface of all the samples was ground by 1200# emery paper. After ultrasound cleaning in alcohol and drying, these samples were immersed into conventional simulated body fluid (c-SBF) with the initial PH of 7.4 at 37 ± 0.2°C. The ratio of solution volume to the surface area was 25 ml: 1 cm^2 according to ASTM G31-72 [38]. The solution was renewed every 48 h. After immersion for 21 days, the samples were washed with CrO_3 solutions for 15 min to remove the corrosion products. The corrosion rates were calculated according to ASTM G31-72 [38].

2.4.2. Polarization test

The cylindrical samples with a length of 20 mm were prepared for

polarization tests. All the samples were ground by 3000# emery paper and then ultrasonic washed in ethanol. The exposed length was 12 mm and the other end was connected to a Cu wire and mounted by silicone rubber. The samples immersed in c-SBF solution at 37 ± 0.2°C were tested through an electrochemical workstation (DH7000, China), which was equipped with a conventional three-electrode system, i.e., a saturated calomel solution as the reference electrode, a platinum sheet as the counter electrode and the sample as the working electrode. In order to obtain a relatively steady electric potential value, open circuit potential (OCP) test was conducted for 30 min firstly. Then the potentio-dynamic polarization was carried out with the voltage ranging from −1.5 V to 1.5 V, and the potentio-dynamic polarization curves were fitted using the Tafel extrapolation method for the calculation of corrosion rate according to ASTM G102-89 [39].

3. Results

3.1. Microstructure characterization

The XRD patterns of as-extruded and as-drawn (with a diameter of 3 mm) Zn-2Cu-0.8Li alloy samples were displayed in Fig. 1. The results revealed that only two groups of characteristic diffraction peaks were clearly detected both in as-extruded and as-drawn samples, which represent the η-Zn phase and the other unknown phase (temporally denoted as α phase hereafter). Herein, the characteristic peaks of the α phase were very close to that of the hexagonal close-packed (hcp) $LiZn_4$ phase studied in many Zn-Li binary alloys [40–42]. Hence, the α phase may also have an hcp crystal structure like the $LiZn_4$ phase. The HCP α phase was identified as the dominated phase in Zn-2Cu-0.8Li alloy due to its stronger peaks than the η-Zn phase. Therefore, the α phase rather than the η-Zn phase is the matrix in Zn-2Cu-0.8Li alloy that is contrary to the other microalloyed Zn alloys [6,10]. Moreover, the α phase including Zn, Cu and Li elements can be almost identified due to the lower solid solubility of Cu and Li in binary Zn-Cu and Zn-Li phase diagrams than alloying contents and the relatively small fraction of η-Zn phase [43]. In addition to the small amount of Cu and Li alloying elements solidly dissolved in the η-Zn phase, the remaining alloying elements formed the α phase with the remaining Zn. Therefore, based on the above results, it is reasonable to define the α phase as (Li, Cu)Zn_4 phase. This (Li, Cu)Zn_4 phase can be considered as the $LiZn_4$ phase with partial substitution of Li atoms by Cu atoms. Similar secondary solid solutions like the (Ag, Cu)Zn_4 phase have been studied by Chen [27].

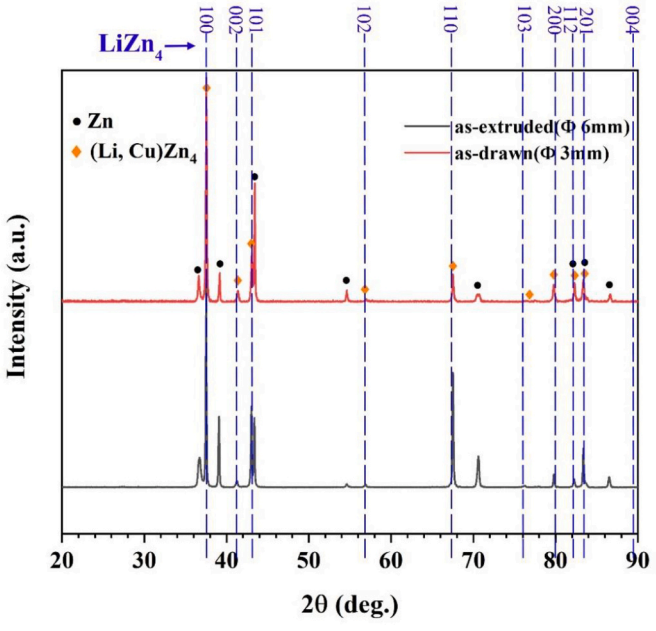

Fig. 1. XRD patterns of as-extruded and as drawn with 75.0% AR Zn-2Cu-0.8Li alloy.

The SEM images and EDS results of as-extruded and as-drawn samples are shown in Fig. 2. The as-extruded sample consisted of the dominant (Li, Cu)Zn_4 phase matrix and dispersive η-Zn phase zones, which exhibit the stripe structure parallel to the extrusion direction. In addition, many needle-like phases with about 1 μm width were diffusely distributed in the (Li, Cu)Zn_4 phase matrix. Fig. 2b–d shows the microstructure of the as-drawn samples. The grains of the (Li, Cu)Zn_4 phase matrix were elongated along the drawing direction and many newly formed particles precipitated in the η-Zn phase after drawing. With the increase in deformation, these phenomena became more evident. Fig. 2e shows the EDS results of three points in Fig. 2a and d. The Cu contents of the (Li, Cu)Zn_4 matrix, η-Zn phase and particle phase are 2.21 wt%, 0.59 wt% and 2.37 wt%, respectively. Moreover, according to the microtopography in Fig. 2a–d, the η-Zn phase region is lower than that of the (Li, Cu)Zn_4 matrix and precipitated particles after the same etching condition. This is probably because the corrosion resistance of the (Li, Cu)Zn_4 phase and particle phase is better than the η-Zn phase due to the higher content of Cu elements with high standard electrode potential.

In order to further determine the phase constitution of the extruded sample, EBSD analysis was performed as shown in Fig. 3a. The crystal parameters of (Li, Cu)Zn_4 phase measured through XRD and referenced the lattice parameters of the $LiZn_4$ phase was imported to the crystal structure library of EBSD and the (Li, Cu)Zn_4 phase (shown in red) and η-Zn phase (shown in blue) were clearly distinguished in the image. It can be clearly observed that the needle-like phase and small amount banded phase were both η-Zn phase while the remaining phase was the (Li, Cu)Zn_4 phase matrix. Since the Li element cannot be detected by EDS, the Li element distribution was measured by the TOFSIMS method (Fig. 3b) to further determine the phase composition. It shows that the Li content in the (Li, Cu)Zn_4 phase matrix and particle phase (marked by the red arrow) is significantly higher than that in the η-Zn phase. Therefore, it can be identified that the matrix phase and particle phase are both Zn-Cu-Li ternary phases. Moreover, according to the XRD pattern of the as-drawn alloy with a diameter of 3 mm, new diffraction peaks do not exist compared to the as-extruded sample. So the composition of these new particles is most probably the (Li, Cu)Zn_4 phase.

In order to study the detailed microstructure of the η-Zn phase and submicron-sized precipitated particles in as-drawn alloys, the microstructure image and selected area diffraction pattern (SADP) of as-drawn alloy with a diameter of 3 mm are shown in Fig. 4. The phase boundary of the matrix phase and DRXed η-Zn zone phase can be easily seen in Fig. 4a and b. The SADP of the DRXed η-Zn phase (marked by yellow arrow) is shown in the inset of Fig. 4b, which can be identified as hcp Zn (a = 0.266 nm, c = 0.495 nm). Besides, the SADP of the matrix (marked by yellow arrow) is likewise shown in the inset of Fig. 4c, which could be demonstrated that the matrix has a set of hcp parameters approaching those of the $LiZn_4$ phase (a = 0.278 nm, c = 0.439 nm). Herein, the matrix shown in Fig. 4c can be almost be proved to be the (Li, Cu)Zn_4 matrix phase. The submicron-sized particle precipitated from the DRXed η-Zn zone can be clearly seen in Fig. 4d. Similarly, its corresponding SADP shown in the inset can also identify as a close hcp crystal structure compared to the $LiZn_4$ phase, which indicates the submicron-sized particle may also be the (Li, Cu)Zn_4 phase.

The EBSD map and inverse pole figures (IPF) for (Li, Cu)Zn_4 matrix and η-Zn phase, both exhibit equiaxed grains, are shown in Fig. 5a. The η-Zn phase was marked separately by the black arrow in IPF maps (Fig. 5a–d). In the as-extruded sample, (Li, Cu)Zn_4 matrix (Fig. 5e) and η-Zn phase (Fig. 5i) both have a fiber texture with the $[\bar{1}2\bar{1}0]$// ED and the maximum intensities are 5.09 and 5.32 mean uniform distribution (MUD), respectively. During drawing, the texture of (Li, Cu)Zn_4 matrix was gradually tilted to $[01\bar{1}0]$ //DD, and the intensity increased

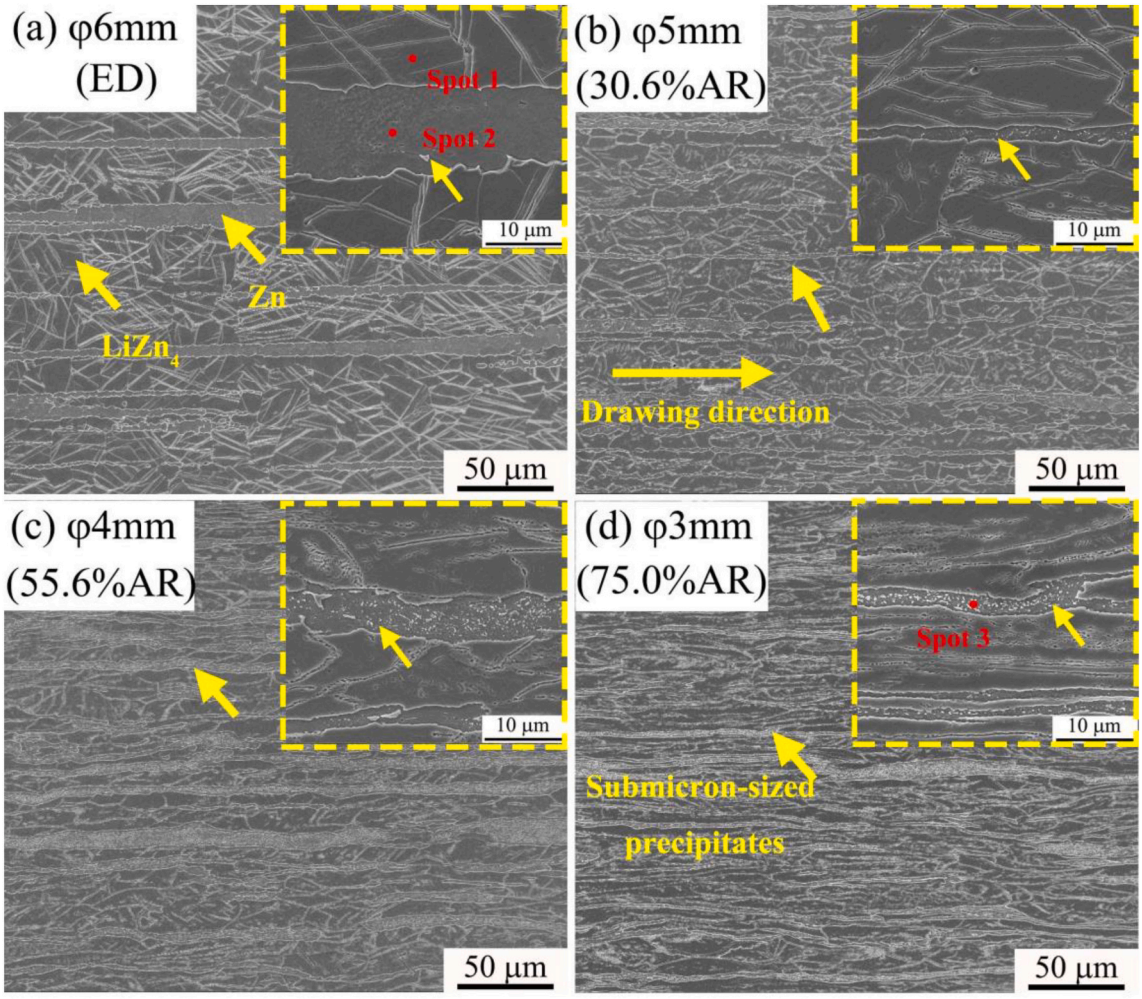

(e)

Elements		Spot 1 (Li, Cu)Zn_4 matrix	Spot 2 η–Zn phase	Spot 3 precipitated particle
Zn	(wt.%)	97.79	99.41	97.63
	(at.%)	97.71	99.40	97.57
Cu	(wt.%)	2.21	0.59	2.37
	(at.%)	2.29	0.60	2.43

Fig. 2. SEM micrographs of as-drawn Zn-2Cu-0.8Li alloy for different degree AR and the high magnification images are also inserted: (a) 0% AR (as-extruded), (b) 30.6% AR, (c) 55.6% AR and (d) 75.0% AR. (e) the EDS results of spots shown in (a) and (d).

continuously, while the texture of the η-Zn phase was tilted from $[\bar{1}2\bar{1}0]$ //ED to [0001] //DD. The maximum intensity of the η-Zn phase increased from 5.32 to 5.75 MUD for 30.6% AR (Fig. 5j), and with deformation further increasing, the maximum intensity was weakened to 2.01 MUD with about a 60° deviation angle from the c axis (Fig. 5k and l).

The statistical results on the grain size of the η-Zn phase during the drawing process are shown in Fig. 6. The grain size gradually decreased from 3.57 μm for the as-extruded sample to 2.34, 1.11 and 0.91 μm for as-drawn samples. The initial grain size of the (Li, Cu)Zn_4 matrix phase was calculated to be 11.54 μm for extruded sample. However, the grain size variation in the drawing of (Li, Cu)Zn_4 matrix was not recorded by EBSD owing to the gradually elongated grains. Moreover, the misorientation angle of the (Li, Cu)Zn_4 matrix is shown in Fig. 7. It can be seen that the volume fraction of low angle grain boundary (LAGB) which is lower than 15°, was persistently increased with the increase of deformation (Fig. 7a–d). However, it shows an opposite trend for the η-Zn phase (Fig. 7e–h).

3.2. Mechanical properties

The tensile tests were conducted on as-extruded and as-drawn samples and their corresponding representative tensile curves are shown in Fig. 8a. Their corresponding UTS, YS and elongation values are presented in Fig. 8b. With the drawing deformation, the ultimate tensile strength (UTS) and the yield strength (YS) continuously increased from

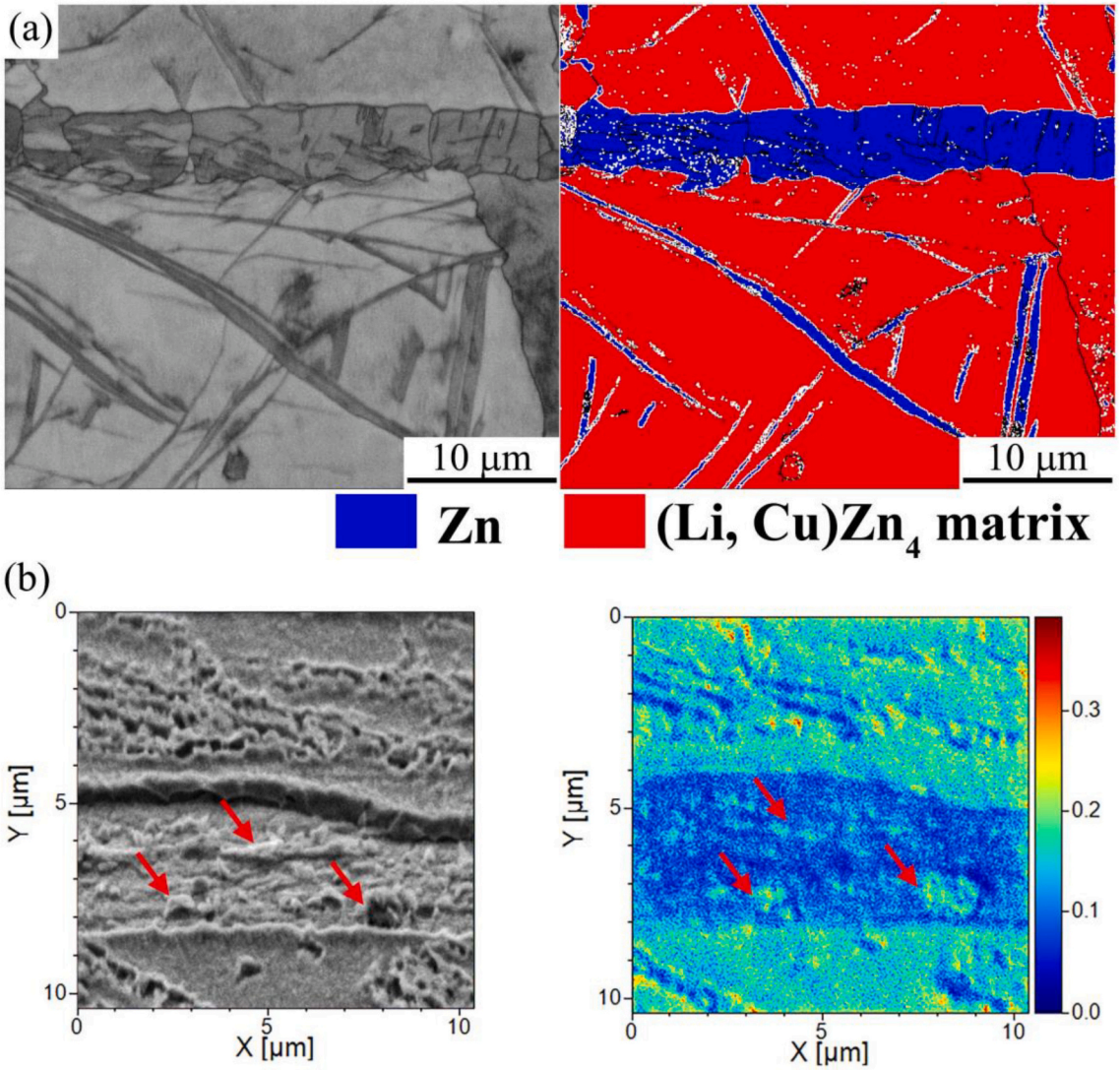

Fig. 3. (a): The image quality and phase map of EBSD for as-extruded Zn-2Cu-0.8Li alloy, (b): the high magnification SEM micrograph of 75.0% AR as-drawn Zn-2Cu-0.8Li alloy with the corresponding map of the Li distribution through TOFSIMS.

348.1 ± 3.1 MPa and 314.2 ± 3.7 MPa for 0% AR to 450.3 ± 8.7 MPa and 417.2 ± 6.8 MPa for 75.0% AR, respectively. However, the elongation firstly increased from 37.1 ± 2.1% for 0% AR to 43.6 ± 2.7% for 30.56.0% AR, but then gradually decreased to 29.5 ± 1.3% for 75% AR. The variation of other parameters like grain size and LAGB density mentioned in Fig. 7 is shown in Fig. 8c. The increasing deformation from drawing resulted in the grain refinement of the η-Zn phase by DRX and the increasing LAGB density of (Li, Cu)Zn_4 matrix. Generally, the increasing drawing deformation resulted in the different microstructure changes on (Li, Cu)Zn_4 matrix and η-Zn phase. The combined influence of the two phases further resulted in changes in mechanical properties during the drawing process.

Since Zn alloys usually exhibit different degrees of aging phenomena and unstable mechanical properties [22], the mechanical properties of the as-drawn sample with 75.0% AR after aging for 6 months at room temperature were also measured, as shown in Fig. 9(a). The tensile strength of the as-drawn sample was only reduced lower than 1.2% and the elongation increased about 8.7% after natural aging, which indicates excellent stability of the mechanical properties during aging at room temperature. Fig. 9(b) and (c) show the SEM micrograph of as-drawn alloy with 75.0% AR and its corresponding samples aged for 6 months, respectively. According to Fig. 9(c), the (Li, Cu)Zn_4 matrix maintained good stability, and there were no second phase particles precipitating from the (Li, Cu)Zn_4 matrix during natural aging.

3.3. Corrosion behavior

In order to investigate the influence of cold drawing on corrosion behavior, the immersion tests and electrochemistry tests were conducted on as-extruded and as-drawn samples. The results of the immersion test in c-SBF are shown in Fig. 10. With the increase in drawing deformation, the average corrosion rate within 21 days gradually increased from 212.07 ± 10.73 μm/year for 0% AR to 309.81 ± 16.53 μm/year for 75.0% AR. The SEM micrographs of as-extruded and as-drawn samples after immersion test are shown in Fig. 10a–d. With the increase in drawing deformation, the content of the corrosion product was more evenly distributed on the alloy surface. The EDS results show that the corrosion products contain O, Zn, P and Ca elements, which are probably ZnO, $Zn(OH)_2$ and phosphates of Zn or Ca, according to the previous studies [44–46]. In addition, the Li-rich corrosion products like LiOH and Li_2CO_3 may exist on the surface oxide film [47].

The Potentio-dynamic polarization curves and parameters calculated through Tafel extrapolation fitting are shown in Fig. 11 and Table 1, respectively. The above curves show that with the increase of drawing

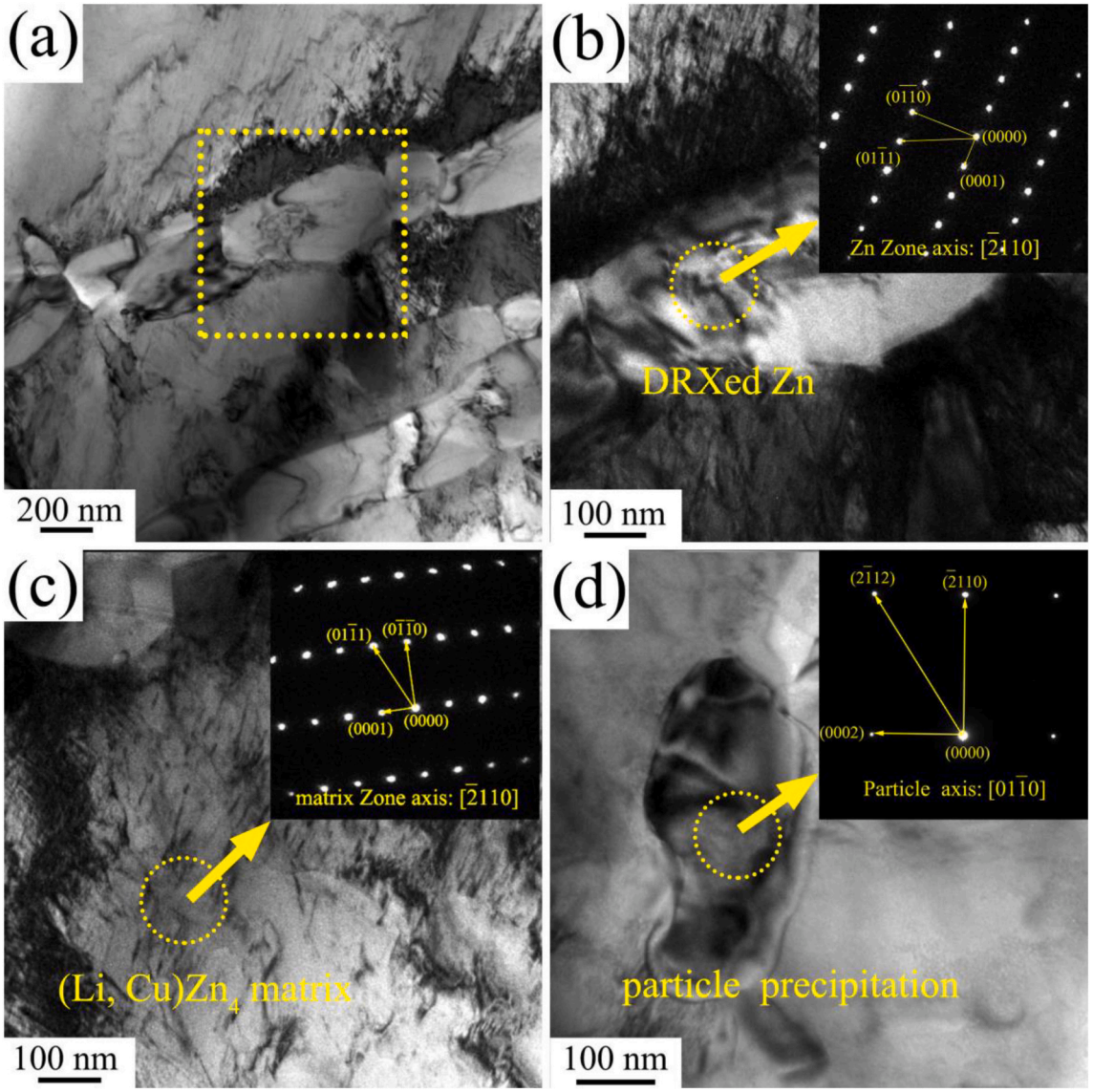

Fig. 4. TEM analysis of as-drawn alloy with 75% AR: (a) TEM graph for low magnification, (b) the high magnification TEM bright field graph of η-Zn phase with it corresponding SADP, (c) the high magnification TEM bright field graph of (Li, Cu)Zn_4 matrix based with it corresponding SADP, (d) the TEM image of particle (Li, Cu)Zn_4 phase and the insert image is corresponding SADP.

deformation, the corrosion potential (V) slightly decreased from −1.168 V for 0% AR to −1.191 V for 75.0% AR. Moreover, the passivation process can be seen in the curves on the anodic branch. With the increase of AR, the passivation process would attenuate gradually and the passive film became less protective. According to the results by Tafel extrapolation fitting, the corrosion current densities (I_{corr}) were gradually increased from 68.278 ± 2.496 μA/cm^2 for 0% AR to 96.425 ± 6.375 μA/cm^2 for 75.0% AR. At the same time, the corrosion rates gradually increased from 0.394 ± 0.016 mm/year for 0% AR to 1.121 ± 0.074 mm /year for 75.0% AR. Although the dynamic corrosion rates tested by the electrochemical method were significantly higher than that of the immersion test and this similar result has been reported in pure Zn wires [4], the overall trend of corrosion rate with drawing deformation is consistent.

4. Discussion

4.1. Effects of cold drawing on microstructure evolution

Owing to Cu and Li's high atomic proportion addition, the as-extruded Zn-2Cu-0.8Li alloy exhibited the particular microstructure where the (Li, Cu)Zn_4 phase (a ternary Zn-Cu-Li intermediate phase compounds) became the matrix. In the previous study, the ternary phase diagram of Zn-Li-Cu alloy was plotted by simulation using the PANDAT software [46], which predicted that the Zn-2Cu-0.8Li alloy had ε-$CuZn_5$ phase, α-$LiZn_4$ phase and Zn phase at room temperature. Actually, in this study, the as-extruded Zn-2Cu-0.8Li alloy had only two phases, i.e. (Li, Cu)Zn_4 phase and η-Zn phase. Herein, the (Li, Cu)Zn_4 phase can be considered an intermediate phase between the $CuZn_5$ phase and the $LiZn_4$ phase whose crystal structure may approach that of the $LiZn_4$ phase rather than the $CuZn_5$ phase due to the higher atomic fraction of Li than that of Cu. In addition, many (Li, Cu)Zn_4 particles were newly precipitated from the η-Zn phase during the cold drawing due to the lower solid solubility of Cu and Li elements at room temperature than that at the extrusion temperature and large deformation. Therefore, the Zn-2Cu-0.8Li alloy with the matrix of (Li, Cu)Zn_4 intermediate phase is different from almost all microalloyed Zn alloys based on the η-Zn phase during cold deformation.

After hot extrusion, the (Li, Cu)Zn_4 matrix and η-Zn phase both exhibited the equiaxed grains structure due to fully dynamic

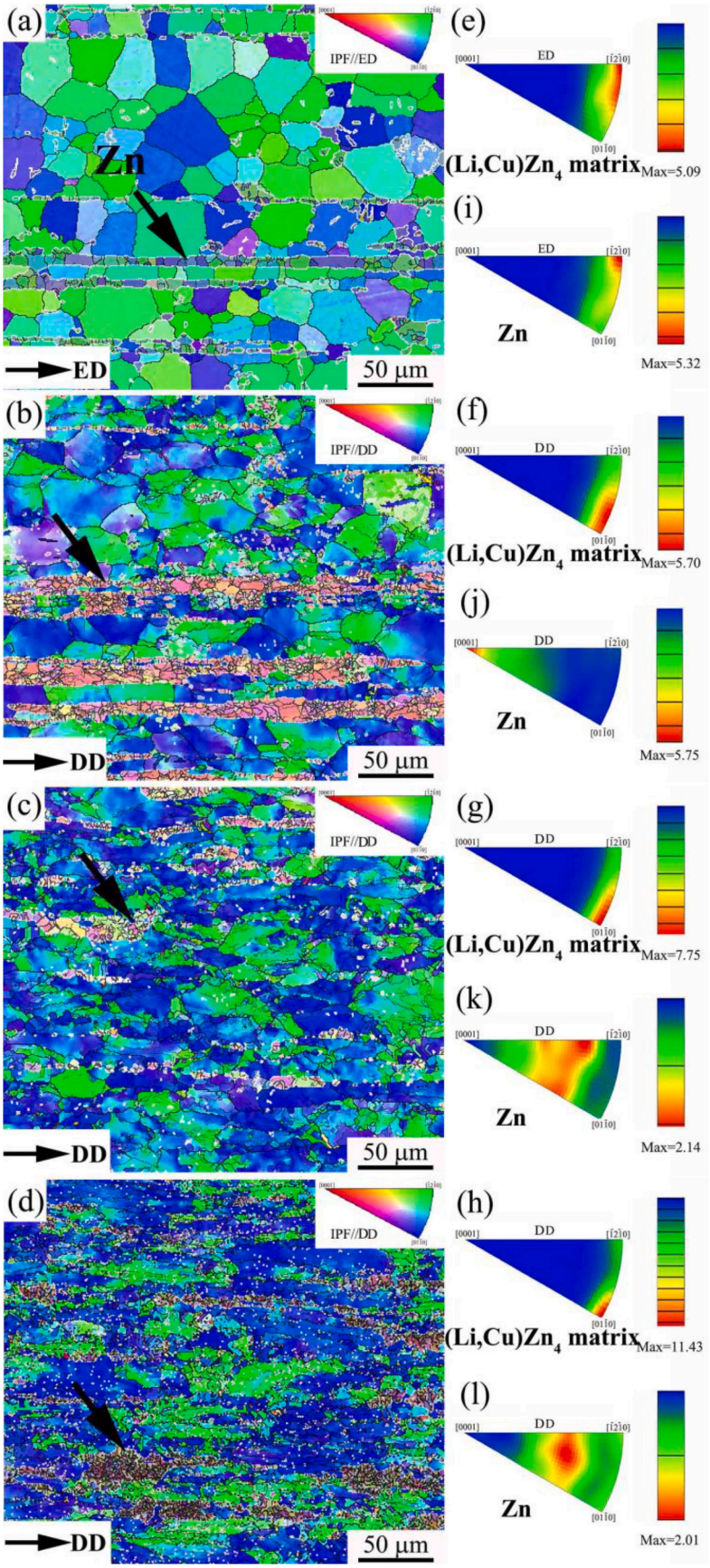

Fig. 5. EBSD maps for different deformation degree of alloy: (a) 0% AR (as-extruded), (b)30.6% AR, (c)55.6% AR and (d) 75.0% AR; inverse pole figures of (Li, Cu) Zn_4 matrix phase for different deformation degree: (e) 0% AR (as-extruded), (f)30.6% AR, (g)55.6% AR and (h) 75.0% AR; inverse pole figures of η-Zn phase for different deformation degree: (i) 0% AR (as-extruded), (j)30.6% AR, (k)55.6% AR and (l) 75.0% AR.

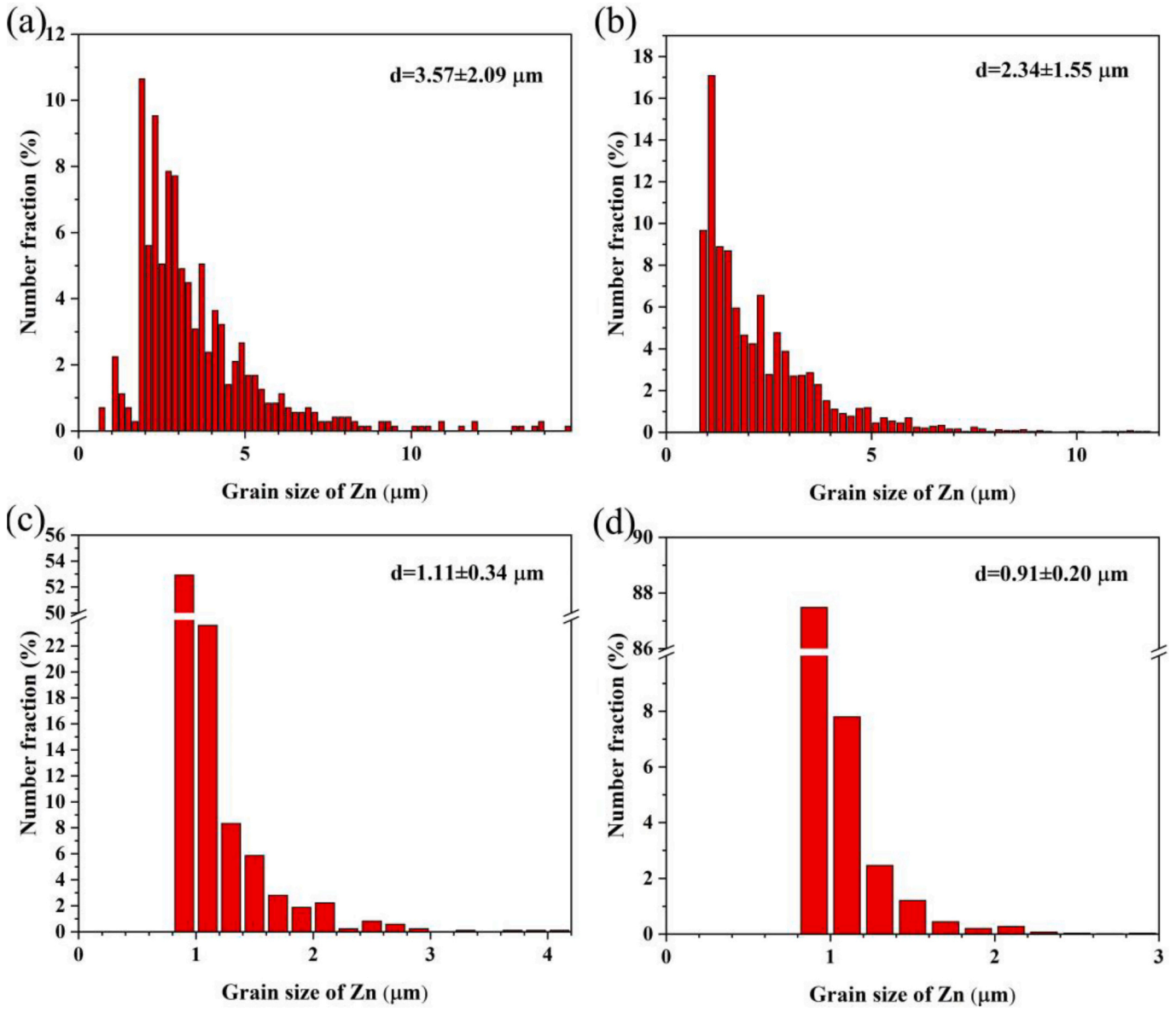

Fig. 6. Grain size statistics of η-Zn phase for different deformation degree: (a) 0% AR (as-extruded), (b) 30.6% AR, (c) 55.6% AR and (d) 75.0% AR.

recrystallization (DRX). After cold drawing, the DRX was constantly occurring in the η-Zn phase due to its low DRX temperature and the grains were further refined. In contrast, the (Li, Cu)Zn_4 matrix phase was only elongated despite massive deformation with no evidence of DRX. According to the binary Zn-Li and Zn-Cu phase diagrams, the $LiZn_4$ and $CuZn_5$ phases both have a higher melting temperature than Zn. The (Li, Cu)Zn_4 matrix phase as the ternary phase including Zn, Cu and Li elements is more likely to possess a higher melting temperature, which indicates a relatively higher recrystallization temperature than room temperature. Moreover, this might also contribute to the difference in texture evolution between the (Li, Cu)Zn_4 matrix phase and η-Zn phase. After hot extrusion at 300°C, (Li, Cu)Zn_4 matrix and η-Zn phase both had a fiber texture with $[\bar{1}2\bar{1}0]$//ED due to the complete DRX. Then when the drawing deformation was conducted from 0% to 35.6%AR, the fraction of $\{10\bar{1}2\}$ twinning boundaries (86.3 ± 5°) calculated from Fig. 7 significantly reduced in the (Li, Cu)Zn_4 matrix phase. It may be because the (Li, Cu)Zn_4 matrix phase has excellent ductility and deformation accommodation by twinning is not needed [48]. The dominant basal dislocation sliding made the initial texture slightly tilt to $[01\bar{1}0]$// DD. In the following drawing, the texture component model of the (Li, Cu)Zn_4 matrix phase did not change due to the invariant dislocation slipping direction but the intensity consistently was enhanced by gradually elongated grains. In order to demonstrate the major basal dislocation slipping, the significant <a > dislocation entanglements were observed in (Li, Cu)Zn_4 matrix phase by two-beam dark-field TEM analysis (Fig. S1 in supplementary data). However, with the combination of relatively high fraction (20%) of $\{10\bar{1}2\}$ twinning boundaries (Fig. 7) and dislocation slip, the texture tilted about 90° from $[\bar{1}2\bar{1}0]$// ED to [0001]//DD in most η-Zn grains at the early drawing stage. Moreover, with the increase in drawing deformation, the DRX with a specific orientation at room temperature continually occurred in the η-Zn phase and formed the new recrystallized texture tilted about 60° away from the [0001] basal plane (Fig. 7g and h). In the η-Zn zone, the (Li, Cu)Zn_4 particles continually precipitated with a low Gibbs free energy [49]. With the increase in drawing deformation, the supersaturated Li and Cu elements were likely segregated at the lattice defects and precipitated from the η-Zn phase [50,51]. These (Li, Cu)Zn_4 particles then became the nucleation sites formed by particle stimulated nucleation (PSN) [52], which gradually weakened the intensity of the new crystallographic texture. The Zn-0.02%Mg alloy [35] had a similar DRX

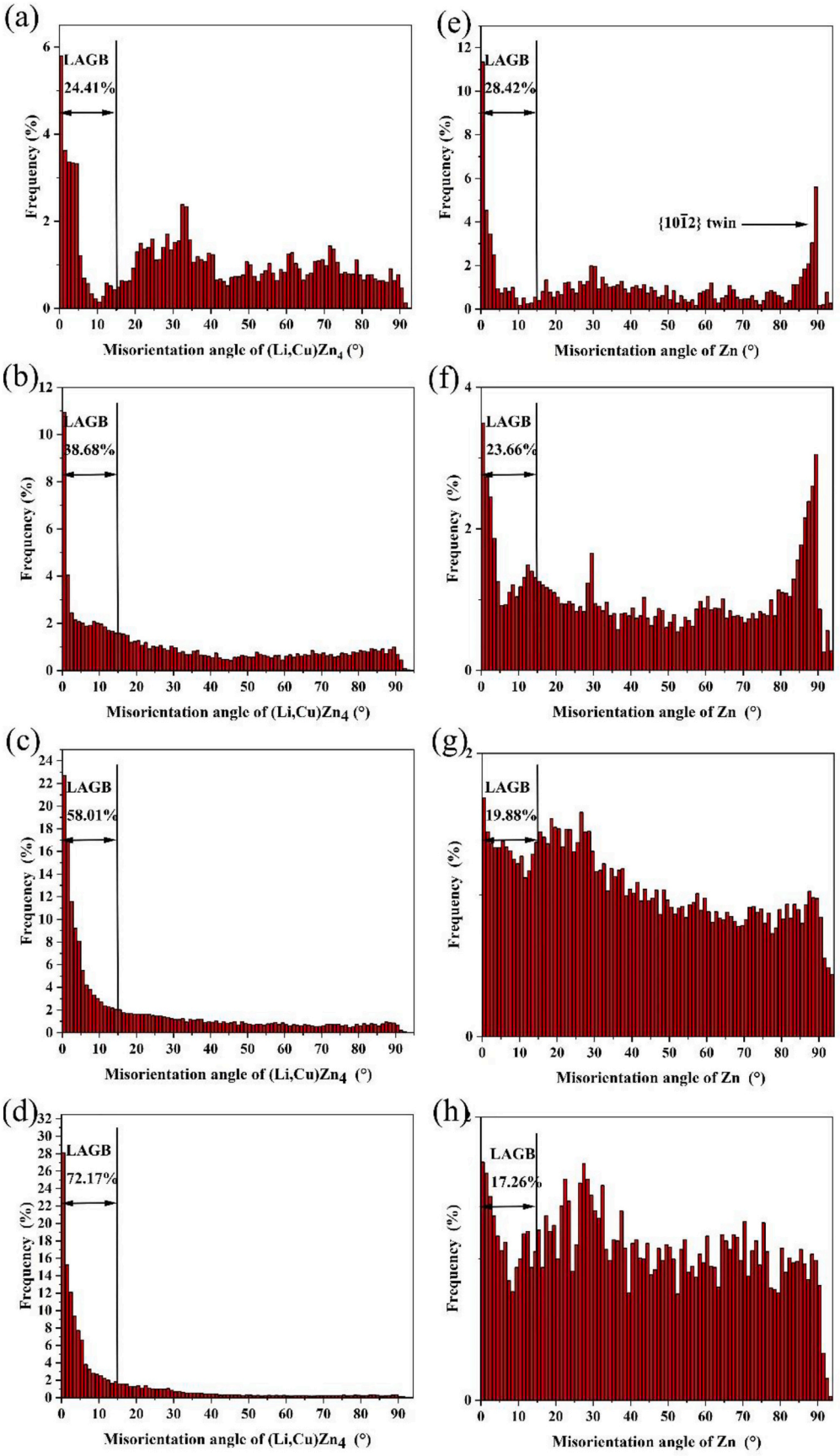

Fig. 7. Misorientation angle of (Li, Cu)Zn_4 matrix phase for different deformation degree: (a) 0% AR (as-extruded), (b) 30.6% AR, (c) 55.6% AR and (d) 75.0% AR; Misorientation angle of η-Zn phase for different deformation degree: (e) 0% AR (as-extruded), (f) 30.6% AR, (g) 55.6% AR and (h) 75.0% AR.

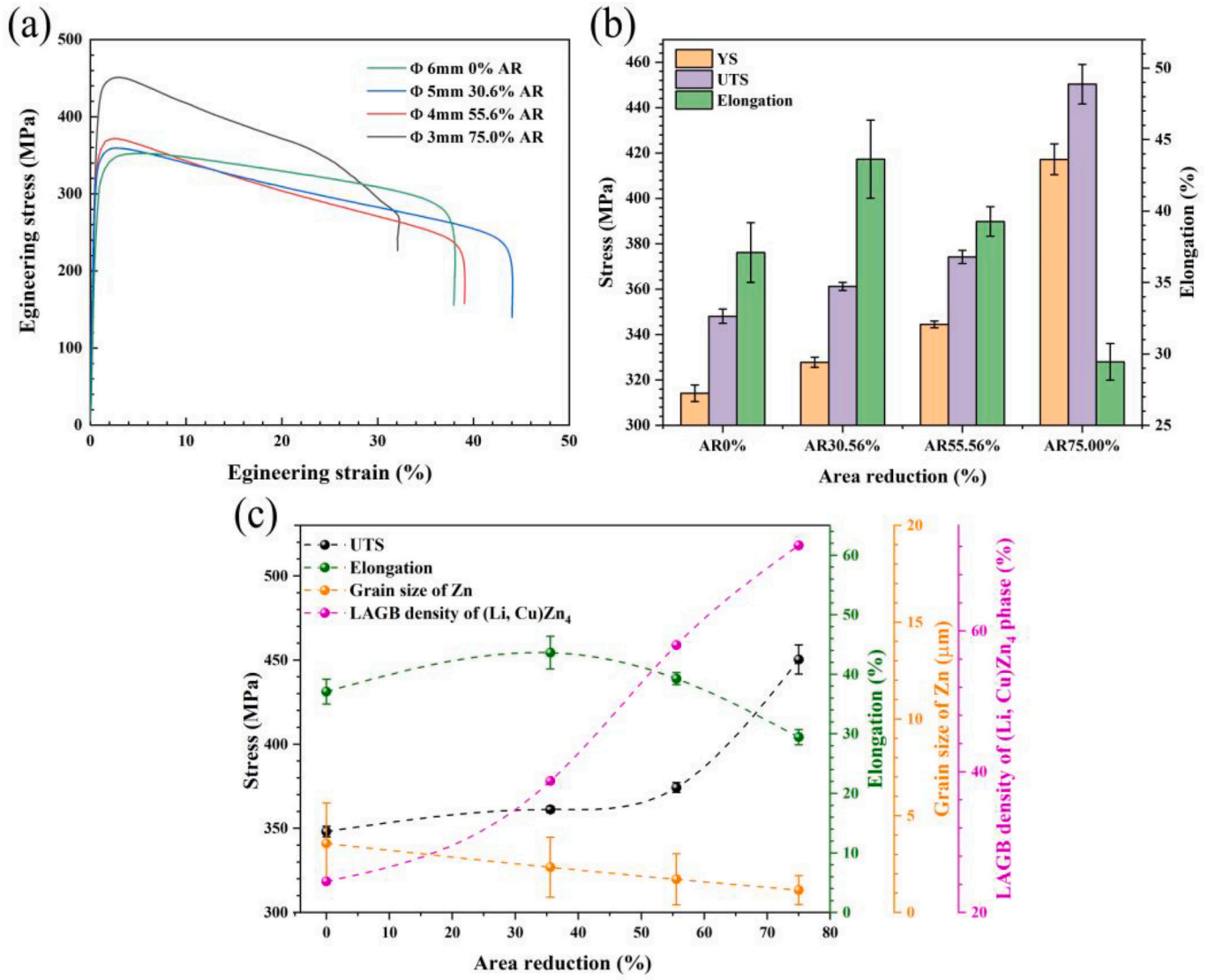

Fig. 8. (a) The tensile curves for the alloy with different amounts of drawing deformation (b) their corresponding YS, UTS and Elongation values, (c) the variation curve of UTS, Elongation, Grain size of Zn and LAGB density of (Li, Cu)Zn_4 matrix phase with AR growth.

texture evolution process during cold drawing due to the PSN.

4.2. *Effects of cold drawing on mechanical properties*

The mechanical properties of Zn-2Cu-0.8Li alloy depend on the joint action of the (Li, Cu)Zn_4 matrix and the η-Zn phase due to its almost dual-phase microstructure. The cold drawing process was acting on the as-extruded samples resulted in different microstructure evolution influences on (Li, Cu)Zn_4 matrix and η-Zn phase. These two phases may together affect the comprehensive mechanical properties of the as-drawn samples.

As for the improved strength of the as-drawn samples, (Li, Cu)Zn_4 matrix played a major strengthening effect due to its dominant volume fraction proportion (84.4 ± 2.4%). The refined grain and secondary phase precipitation resulting in the DRX softening in the η-Zn phase are not dominant here [53]. The grains of the (Li, Cu)Zn_4 matrix were continually elongated, resulting in dislocation pile up and increasing texture intensity in the (Li, Cu)Zn_4 matrix. The work hardening caused by dislocation accumulation and tangling during the grain elongating of (Li, Cu)Zn_4 matrix and texture effects were the primary strengthening mechanism during cold drawing. With the increase in dislocation pileup and texture intensity, the fraction of the LAGB in (Li, Cu)Zn_4 matrix continually increased. Therefore, the fraction variation for the LAGB in (Li, Cu)Zn_4 matrix can quantify the reinforcement effects caused by dislocation pileup and enhanced fiber texture. Hence, the strengthening degree of (Li, Cu)Zn_4 matrix phase can be roughly summarized by LAGB and HAGB and it can be explained by the following Eq. [54]:

$$\Delta\sigma_{LAGB} = M\alpha Gb\sqrt{\rho_0 + 3f\overline{\theta}_{LAGB}/(bL)} \quad (2)$$

$$\Delta\sigma_{HAGB} = k\sqrt{(1-f)/L} \quad (3)$$

where the α (0.2) and M (about 3.1) are a constant, G is shear modulus, b is burgers vector, ρ_0 is primary dislocation density in the phase boundary (Li, Cu)Zn_4 matrix phase before drawing, L is spacing between phase boundary of (Li, Cu)Zn_4 matrix, f is the fraction of LAGB, $\overline{\theta}_{LAGB}$ is the average misorientation angle of LAGB and k is the slope of corresponding Hall-Petch. According to the above equation and Fig. 7, the LAGB in the (Li, Cu)Zn_4 matrix phase gradually contributed the more strengthen effects in the strength increment in the later drawing stages due to its high fraction.

As for the plasticity of as-drawn Zn-2Cu-0.8Li alloy, its integral ductility depends on the individual ductility of (Li, Cu)Zn_4 matrix and η-Zn phase and the compatible deformation capability between them.

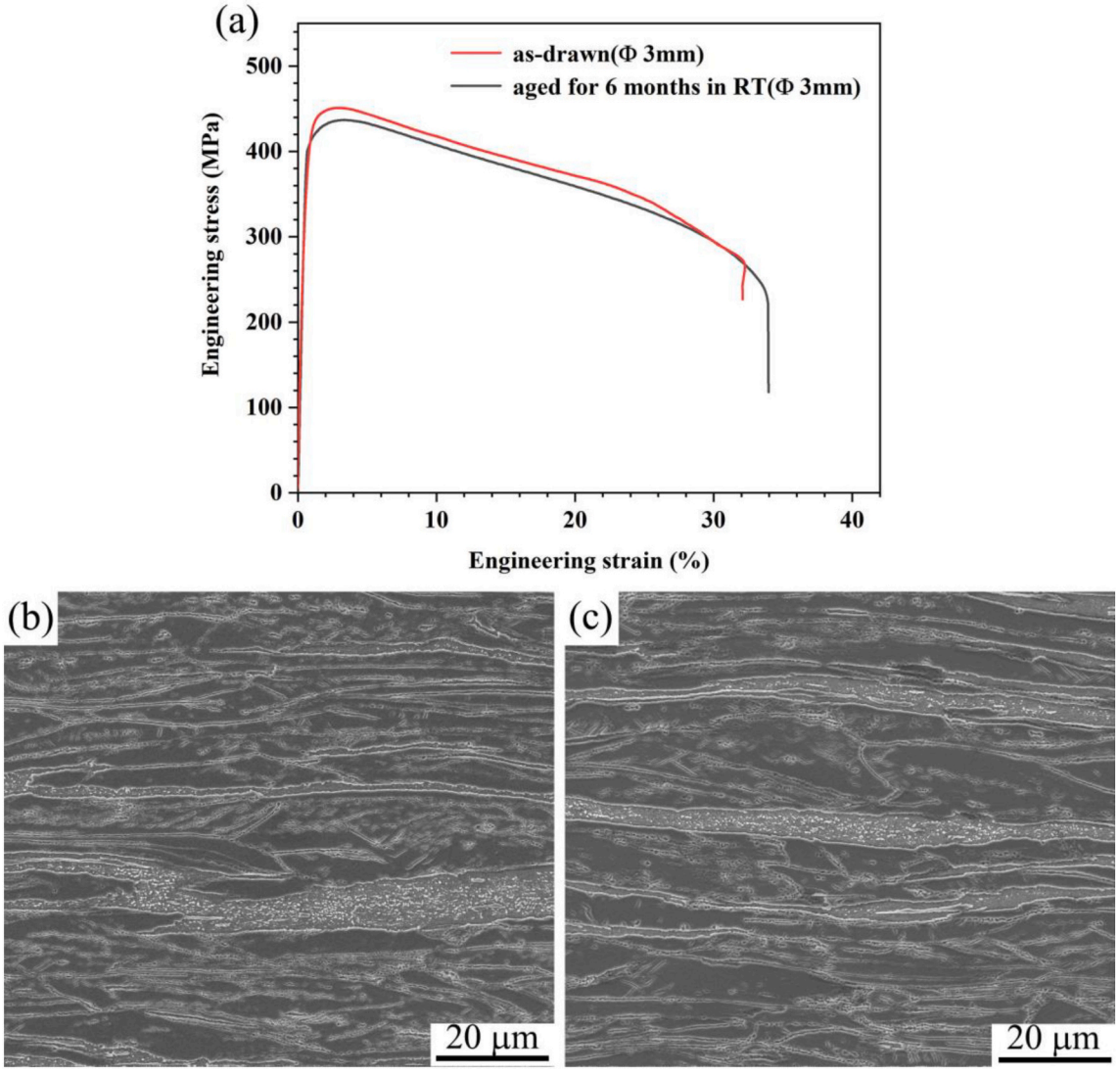

Fig. 9. (a) Representative tensile engineering stress-engineering strain curves of the as-drawn alloy with 75.0% AR and its corresponding samples for 6 months' storage time, (b) SEM micrograph of as-drawn alloy with 75.0% AR, (c) SEM micrograph of as-drawn alloy with 75.0% AR aged for 6 months.

The substantially elongated grains of the (Li, Cu)Zn_4 matrix was the result of its sufficient ductility in the initial state. However, with the increase in drawing deformation, the work hardening and residual stresses in (Li, Cu)Zn_4 matrix due to grain elongation would significantly reduce its ductility. In addition, Huang et al. [55] found that with the deformation texture tilting from $[\bar{1}2\bar{1}0]$//ED to $[01\bar{1}0]$//DD for hcp Mg alloy, it became more difficult for dislocation sliding. Therefore, both texture change and work hardening can lead it difficulties for (Li, Cu)Zn_4 matrix deformation. On the contrary, the increase in drawing deformation induced the gradual DRX and grain refinement in the η-Zn phase, which can improve its ductility. In general, the basal $\{0001\}<11\bar{2}0>$ dislocation slipping and $\{10\bar{1}2\}$ twinning are the main deformation methods at room temperature in the Zn grains [56]. With the decrease in grain size to critical grain size (about several μm) during cold drawing, the other dislocation slip systems were more likely activated rather than twinning [57], especially pyramidal $\{11\bar{2}2\}<11\bar{2}3>$ dislocation slip. The decreasing fraction of $\{10\bar{1}2\}$ twin boundaries ($86.3 \pm 5°$) from 21% for 0% AR to 9% for 75.0% AR calculated from Fig. 7 can demonstrate the decreasing ratio on deformation in the η-Zn phase, which is favorable to improve ductility. Meanwhile, with the increase of total crystal boundary length, grain boundary sliding occurred more easily in the η-Zn phase and this further resulted in the increasing ductility of the η-Zn phase. Moreover, the (Li, Cu)Zn_4 particles phase substantially participating from the η-Zn phase may result in precipitate softening due to phase boundary sliding which had been identified in many Zn alloys [21,53]. Herein, with the increase of drawing deformation, the ductility of the (Li, Cu)Zn_4 matrix decreased while the ductility of the η-Zn phase was continually improved. So in the early drawing stages, combining the excellent compatible deformation capability of the η-Zn phase, the integral ductility of the as-drawn sample was improved inversely. In order to investigate the details of these two phases' compatible deformation situation in the tensile test, the microstructure near the fracture surface of tested samples is shown in Fig. 12. It can be clearly seen that the η-Zn phase converged in the fracture region and appeared closed to necking. With the increase in drawing deformation in the early stage, the significant DRX that occurred in the η-Zn phase near the fracture resulted in the increase in elongation. However, with further drawing to 75.0% AR, the strength mismatch between the (Li, Cu)Zn_4 matrix and η-Zn phase resulted in the crack appearing at the phase boundaries (Fig. 12d). Therefore, the elongation of the as-drawn sample with 75.0% AR decreased significantly after further drawing.

In addition, the mechanical properties of the as-drawn Zn-2Cu-0.8Li samples after natural aging for 6 months were basically stable, avoiding

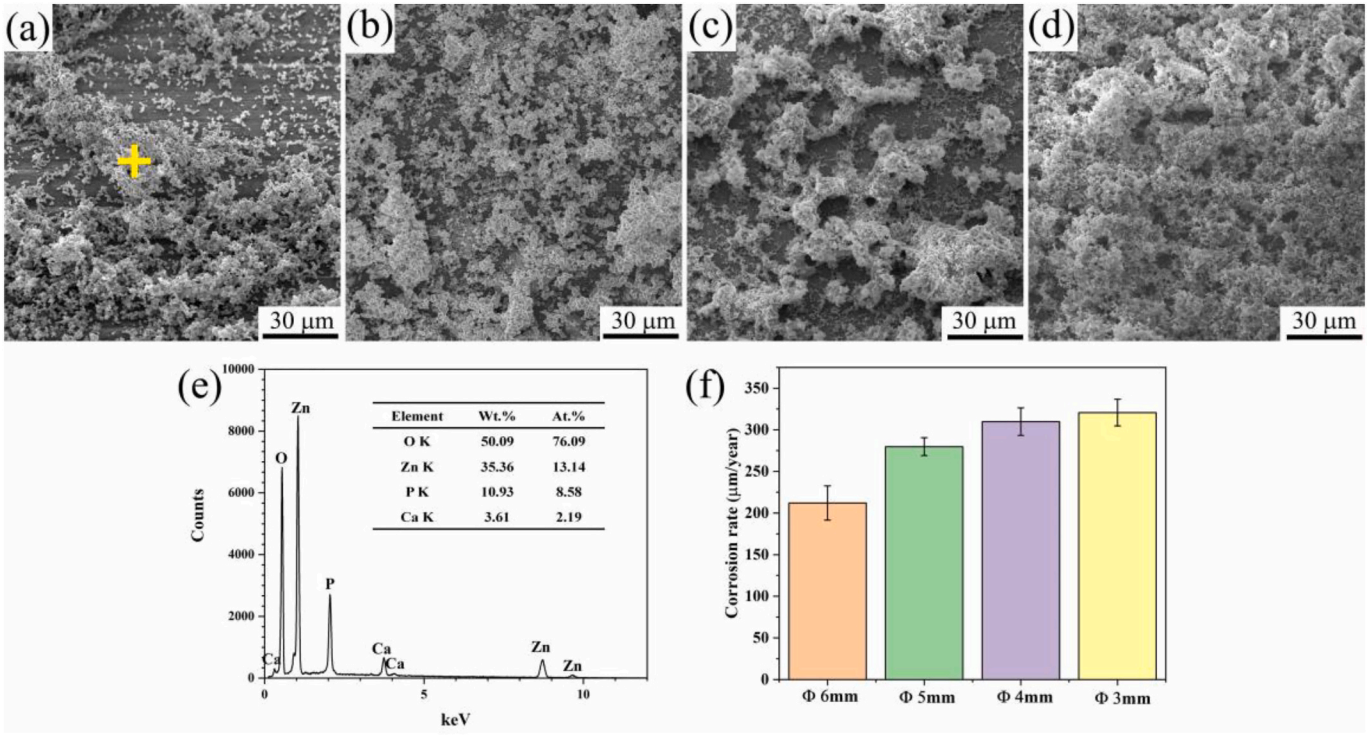

Fig. 10. The SEM micrograph after immersion of different drawing deformation alloy for: (a) 0%AR. (b) 30.6%AR, (c) 55.6%AR and (d) 75.0%AR; (e) EDS result for yellow point in (a). (f) their corresponding corrosion rate within 21 days. (For interpretation of the references to colour in this figure legend, the reader is referred to the web version of this article.)

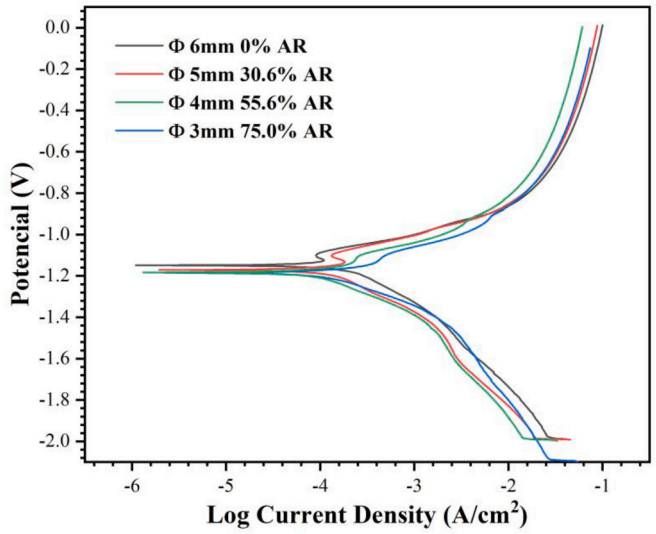

Fig. 11. Potentio-dynamic polarization curve of different drawing deformation alloy.

the aging problem that appeared in Zn-Mg and Zn-Li alloys [22,58]. This is because the dominant (Li, Cu)Zn_4 matrix present in as-drawn samples had a relatively high thermodynamic stability compared to the η-Zn phase. The slight dislocation recovery in the (Li, Cu)Zn_4 matrix may be the primary reason for the little decline of strength and increase in ductility. Therefore, the as-drawn Zn-2Cu-0.8Li can maintain mechanical stability at room temperature for a rather long time.

4.3. Effects of cold drawing on corrosion behavior

The corrosion rates of the Zn-2Cu-0.8Li alloy with different drawing deformation in c-SBF were around 200–320 μm/year, significantly higher than most Zn-based alloys [59]. This may be attributed to two major reasons: (1) extensive micro-galvanic coupling corrosion; (2) forming intensive defects after cold drawing such as dislocation. According to the microstructure of these test samples after acid pickling, the electrode potential of the (Li, Cu)Zn_4 matrix and particle phase was higher than that of the η-Zn phase, leading to micro-galvanic corrosion. Moreover, with the increase in cold drawing deformation, the (Li, Cu)Zn_4 particles further precipitated from the η-Zn phase would increase the phase boundaries. Hence, the increasing phase boundaries can accelerate the integral corrosion rate. In addition, after drawing, dislocation accumulated in the grain boundary of (Li, Cu)Zn_4 matrix phase and formed the high energy low angle grain boundaries [60]. On the one hand, the formation of defects can accelerate diffusion and stress corrosion. On the other hand, it is adverse to the formation of passivation film and ultimately leads to accelerated corrosion. Therefore, the corrosion rates of the Zn-2Cu-0.8Li alloy increased with the drawing deformation. However, although the corrosion rate increases to 309.81 ± 16.53 μm/year for 75.0% AR, this rate is well suited to the degradation rate required for clinical applications [59].

Table 1
Corresponding fitting parameters by Tafel extrapolation.

Diameter of Zn2Cu0.8Li wires	E_{corr}(V_{SEC})	I_{corr}(μA/cm^2)	βa(mV/decade)	βc(-mV/decade)	Corrosion rate (mm/year)
6 mm	−1.169 ± 0.012	68.278 ± 2.496	42.380 ± 4.206	91.133 ± 6.711	0.394 ± 0.016
5 mm	−1.183 ± 0.011	81.305 ± 4.356	43.975 ± 4.004	104.079 ± 5.566	0.555 ± 0.043
4 mm	−1.188 ± 0.008	93.455 ± 8.045	43.944 ± 4.032	109.85 ± 2.459	0.898 ± 0.028
3 mm	−1.190 ± 0.014	96.425 ± 6.375	36.348 ± 1.836	146.999 ± 16.001	1.121 ± 0.074

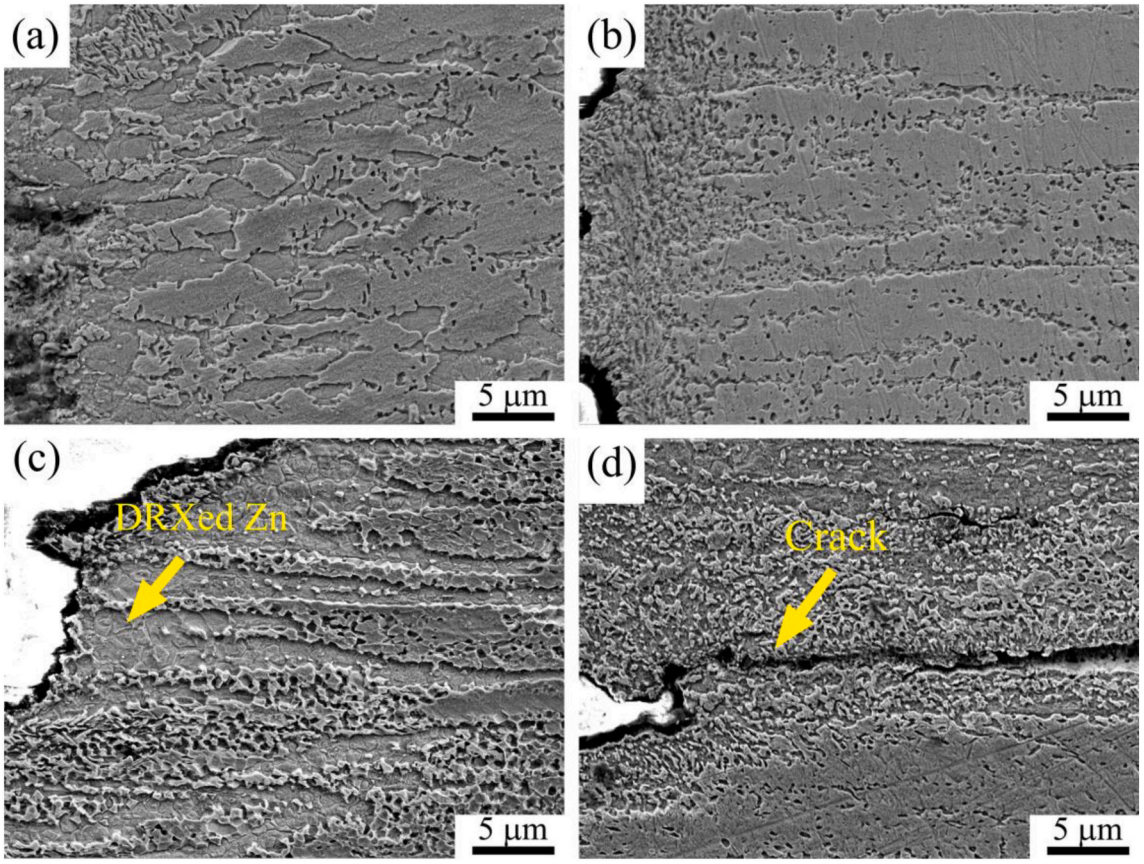

Fig. 12. Microstructure near the fracture after tensile test of different drawing deformation: (a) 0%AR. (b) 30.6%AR, (c) 55.6%AR and (d) 75.0%AR.

5. Conclusions

In this study, Zn-2Cu-0.8Li wires with high strength and ductility were developed by multiple pass cold drawing. The effects of cold drawing on microstructure evolution, mechanical properties and corrosion behavior were studied and discussed, and the following conclusions can be obtained:

1. The as-extruded Zn-2Cu-0.8Li alloy contains the dominant (Li, Cu)Zn_4 matrix phase (84.4 ± 2.4% volume fraction) and η-Zn phase. During cold drawing, the (Li, Cu)Zn_4 matrix phase was continuously elongated, while the η-Zn phase was significantly refined due to DRX with newly precipitated (Li, Cu)Zn_4 particles. The hcp (Li, Cu)Zn_4 phase, a Zn-Cu-Li ternary phase, had crystallographic parameters approaching those of the $LiZn_4$ phase.
2. After cold drawing, $[01\bar{1}0]$//DD fiber texture with high intensity formed for the (Li, Cu)Zn_4 matrix while the typical weak DRX texture with about 60° angle tilted from [0001] formed for the η-Zn phase.
3. The deformation associated with drawing improved, the mechanical strength sharply from YS 314.2 ± 3.7 MPa and UTS 348.1 ± 3.1 MPa of the as-extruded alloy to YS 417.2 ± 6.8 MPa and UTS 450.3 ± 8.7 MPa (75% AR), while the elongation decreased from 37.1 ± 2.1% to 29.5 ± 1.3%. The (Li, Cu)Zn_4 matrix played a major strengthening effect and the softened η-Zn phase zone showed an excellent ability to accommodate the deformation which maintained the certain integral ductility of the as-drawn samples.
4. The as-drawn Zn-2Cu-0.8Li alloy was basically stable in 6 months of natural aging due to the excellent thermostability of (Li, Cu)Zn_4 matrix.
5. The corrosion rates of as-drawn samples were around 210–310 μm/year. With the increase in drawing deformation, the corrosion rate increased due to extensive micro-galvanic coupling corrosion and intensive defects.

Data availability statement

The raw/processed data used to support the findings of this study has not been made available because the data also forms part of an ongoing study.

Declaration of Competing Interest

The authors declare that they have no known competing financial interests or personal relationships that could have appeared to influence the work reported in this paper.

Acknowledgments

This work was supported by the National Key Research and Development Program of China (No. 2018YFE0115400), the National Natural Science Foundation of China (No. 51971134 and 52101290), Shanghai International Joint-Innovation Program (No. 20520711700) and Shanghai Jiao Tong University Medial-Engineering Cross Fund (ZH2018ZDA34 and YG2019ZDA02).

Appendix A. Supplementary data

Supplementary data to this article can be found online at https://doi.org/10.1016/j.matchar.2022.111722.

References

[1] J. Frattolin, E. Cattarinuzzi, S. Rajagopalan, D. Gastaldi, P. Vena, S. Yue, O. Bertrand, R. Mongrain, Development of a micro-scale method to assess the effect of corrosion on the mechanical properties of a biodegradable Fe-316L stent material, J. Mech. Behav. Biomed. Mater. 114 (2021) 104173.
[2] V. Tsakiris, C. Tardei, F. Clicinschi, Biodegradable Mg alloys for orthopedic implants - a review, J. Magnes. Alloys (2021).
[3] H. Li, Z. Shi, L. Wang, Opportunities and challenges of biodegradable Zn-based alloys, J. Mater. Sci. Technol. 46 (2020) 136–138.
[4] H. Guo, R. Cao, Y. Zheng, J. Bai, F. Xue, C. Chu, Diameter-dependent in vitro performance of biodegradable pure zinc wires for suture application, J. Mater. Sci. Technol. 35 (8) (2019) 1662–1670.
[5] E. Mostaed, M. Sikora-Jasinska, J. Drelich, M. Vedani, Zinc-based alloys for degradable vascular stent applications, Acta Biomater. 71 (2018) 1–23.
[6] J. Jiang, H. Huang, J. Niu, Z. Jin, M. Dargusch, G. Yuan, Characterization of nano precipitate phase in an as-extruded Zn-Cu alloy, Scr. Mater. 200 (2021) 113907.
[7] J. Niu, Z. Tang, H. Huang, J. Pei, H. Zhang, G. Yuan, W. Ding, Research on a Zn-Cu alloy as a biodegradable material for potential vascular stents application, Mater. Sci. Eng. C 69 (2016) 407–413.
[8] J. Sun, X. Zhang, Z. Shi, X. Gao, X. Liu, J. Wang, L. Wang, Adjusting comprehensive properties of biodegradable Zn-Mn alloy through solution heat-treatment, Mater. Today Commun. 23 (2020) 101150.
[9] P. Sotoudeh-Bagha, S. Khaleghpanah, S. Sheibani, M. Khakbiz, A. Zakeri, Characterization of nanostructured biodegradable Zn-Mn alloy synthesized by mechanical alloying, J. Alloys Compd. 735 (2018) 1319–1327.
[10] M. Sikora-Jasinska, E. Mostaed, A. Mostaed, R. Beanland, D. Mantovani, M. Vedani, Fabrication, mechanical properties and in vitro degradation behavior of newly developed ZnAg alloys for degradable implant applications, Mater. Sci. Eng. C 77 (2017) 1170–1181.
[11] M. Watroba, W. Bednarczyk, J. Kawalko, K. Mech, M. Marciszko, G. Boelter, M. Banzhaf, P. Bala, Design of novel Zn-Ag-Zr alloy with enhanced strength as a potential biodegradable implant material, Mater. Des. 183 (2019) 108154.
[12] J. He, D. Li, F. He, Y. Liu, Y. Liu, C. Zhang, F. Ren, Y. Ye, X. Deng, D. Yin, A study of degradation behaviour and biocompatibility of Zn-Fe alloy prepared by electrodeposition, Mater. Sci. Eng. C 117 (2020) 111295.
[13] Z. Shi, X. Gao, H. Chen, X. Liu, A. Li, H. Zhang, L. Wang, Enhancement in mechanical and corrosion resistance properties of a biodegradable Zn-Fe alloy through second phase refinement, Mater. Sci. Eng. C 116 (2020) 111197.
[14] G. Li, S. Zhu, J. Nie, Y. Zheng, Z. Sun, Investigating the stress corrosion cracking of a biodegradable Zn-0.8 wt%Li alloy in simulated body fluid, Bioact. Mater. 6 (5) (2021) 1468–1478.
[15] Y. Dai, Y. Zhang, H. Liu, H. Fang, D. Li, X. Xu, Y. Yan, L. Chen, Y. Lu, K. Yu, Mechanical strengthening mechanism of Zn-Li alloy and its mini tube as potential absorbable stent material, Mater. Lett. 235 (2019) 220–223.
[16] X. Shao, X. Wang, F. Xu, T. Dai, J.G. Zhou, J. Liu, K. Song, L. Tian, B. Liu, Y. Liu, In vivo biocompatibility and degradability of a Zn-Mg-Fe alloy osteosynthesis system, Bioact. Mater. 7 (2022) 154–166.
[17] W. Pachla, S. Przybysz, A. Jarzebska, M. Bieda, K. Sztwiertnia, M. Kulczyk, J. Skiba, Structural and mechanical aspects of hypoeutectic Zn-Mg binary alloys for biodegradable vascular stent applications, Bioact. Mater. 6 (1) (2021) 26–44.
[18] Y. Zou, X. Chen, B. Chen, Effects of Ca concentration on degradation behavior of Zn-xCa alloys in Hank's solution, Mater. Lett. 218 (2018) 193–196.
[19] B. Jia, H. Yang, Z. Zhang, X. Qu, X. Jia, Q. Wu, Y. Han, Y. Zheng, K. Dai, Biodegradable Zn-Sr alloy for bone regeneration in rat femoral condyle defect model: in vitro and in vivo studies, Bioact. Mater. 6 (6) (2021) 1588–1604.
[20] H. Yang, B. Jia, Z. Zhang, X. Qu, G. Li, W. Lin, D. Zhu, K. Dai, Y. Zheng, Alloying design of biodegradable zinc as promising bone implants for load-bearing applications, Nat. Commun. 11 (1) (2020) 401.
[21] M. Watroba, W. Bednarczyk, J. Kawalko, P. Bala, Fine-tuning of mechanical properties in a Zn-Ag-Mg alloy via cold plastic deformation process and post-deformation annealing, Bioact. Mater. 6 (10) (2021) 3424–3436.
[22] H. Jin, S. Zhao, R. Guillory, P.K. Bowen, Z. Yin, A. Griebel, J. Schaffer, E.J. Earley, J. Goldman, J.W. Drelich, Novel high-strength, low-alloys Zn-Mg (<0.1wt% Mg) and their arterial biodegradation, Mater. Sci. Eng. C 84 (2018) 67–79.
[23] Z. Tang, J. Niu, H. Huang, H. Zhang, J. Pei, J. Ou, G. Yuan, Potential biodegradable Zn-Cu binary alloys developed for cardiovascular implant applications, J. Mech. Behav. Biomed. Mater. 72 (2017) 182–191.
[24] Y. Qian, G. Yuan, Research status, challenges, and countermeasures of biodegradable zinc-based vascular stents, Acta Metall. Sin. 57 (3) (2021) 272–282.
[25] X. Qu, H. Yang, B. Jia, Z. Yu, Y. Zheng, K. Dai, Biodegradable Zn-Cu alloys show antibacterial activity against MRSA bone infection by inhibiting pathogen adhesion and biofilm formation, Acta Biomater. 117 (2020) 400–417.
[26] C. Zhou, H. Li, Y. Yin, Z. Shi, T. Li, X. Feng, J. Zhang, C. Song, X. Cui, K. Xu, Y. Zhao, W. Hou, S. Lu, G. Liu, M. Li, J. Ma, E. Toft, A. Volinsky, M. Wan, X. Yao, C. Wang, K. Yao, S. Xu, H. Lu, S. Chang, J. Ge, L. Wang, H. Zhang, Long-term in vivo study of biodegradable Zn-Cu stent: a 2-year implantation evaluation in porcine coronary artery, Acta Biomater. 97 (2019) 657–670.
[27] C. Chen, R. Yue, J. Zhang, H. Huang, J. Niu, G. Yuan, Biodegradable Zn-1.5Cu-1.5Ag alloy with anti-aging ability and strain hardening behavior for cardiovascular stents, Mater. Sci. Eng. C 116 (2020) 111172.
[28] R. Yue, J. Niu, Y. Li, G. Ke, H. Huang, J. Pei, W. Ding, G. Yuan, In vitro cytocompatibility, hemocompatibility and antibacterial properties of biodegradable Zn-Cu-Fe alloys for cardiovascular stents applications, Mater. Sci. Eng. C 113 (2020) 111007.
[29] Z. Tang, H. Huang, J. Niu, L. Zhang, H. Zhang, J. Pei, J. Tan, G. Yuan, Design and characterizations of novel biodegradable Zn-Cu-Mg alloys for potential biodegradable implants, Mater. Des. 117 (2017) 84–94.
[30] C. Chen, S. Fan, J. Niu, H. Huang, Z. Jin, L. Kong, D. Zhu, G. Yuan, Alloying design strategy for biodegradable zinc alloys based on first-principles study of solid solution strengthening, Mater. Des. 204 (2021) 109676.
[31] W. Young, Review of lithium effects on brain and blood, Cell Transplant. 18 (9) (2009) 951–975.
[32] S. Zhao, C. McNamara, P. Bowen, N. Verhun, J. Braykovich, J. Goldman, J. Drelich, Structural characteristics and in vitro biodegradation of a novel Zn-Li alloy prepared by induction melting and hot rolling, Metall. Mater. Trans. A 48 (3) (2017) 1204–1215.
[33] G. Mao, C. Wang, M. Feng, B. Wen, S. Yu, X. Han, Z. Yu, Y. Qiu, W. Bian, Effect of biodegradable Zn screw on bone tunnel enlargement after anterior cruciate ligament reconstruction in rabbits, Mater. Des. 207 (2021) 109834.
[34] J. Raiha, Biodegradable implants as intramedullary nails. A survey of recent studies and an introduction to their use, Clin. Mater. 10 (1) (1992) 35–39.
[35] L. Wang, Y. He, H. Zhao, H. Xie, S. Li, Y. Ren, G. Qin, Effect of cumulative strain on the microstructural and mechanical properties of Zn-0.02 wt%Mg alloy wires during room-temperature drawing process, J. Alloys Compd. 740 (2018) 949–957.
[36] E. Mostaed, M. Sikora-Jasinska, M. Ardakani, A. Mostaed, I. Reaney, J. Goldman, J. Drelich, Towards revealing key factors in mechanical instability of bioabsorbable Zn-based alloys for intended vascular stenting, Acta Biomater. 105 (2020) 319–335.
[37] ASTM E8/E8M-16a, Standard test methods for tension testing of metallic materials, ASTM Int. (2016) 1–28.
[38] ASTM NACE/ASTMG31-12a, Standard guide for laboratory immersion corrosion testing of metals, ASTM Int. (2012) 1–9.
[39] ASTM, G102-89, standard practice for calculation of corrosion rates and related information from electrochemical measurements, ASTM Int. (2015) 1–7.
[40] Z. Li, Z. Shi, Y. Hao, H. Li, H. Zhang, X. Liu, L. Wang, Insight into role and mechanism of Li on the key aspects of biodegradable ZnLi alloys: microstructure evolution, mechanical properties, corrosion behavior and cytotoxicity, Mater. Sci. Eng. C 114 (2020) 111049.
[41] Z. Li, Z. Shi, Y. Hao, H. Li, X. Liu, A. Volinsky, H. Zhang, L. Wang, High-performance hot-warm rolled Zn-0.8Li alloy with nano-sized metastable precipitates and sub-micron grains for biodegradable stents, J. Mater. Sci. Technol. 35 (11) (2019) 2618–2624.
[42] Y. Zhang, Y. Yan, X. Xu, Y. Lu, L. Chen, D. Li, Y. Dai, Y. Kang, K. Yu, Investigation on the microstructure, mechanical properties, in vitro degradation behavior and biocompatibility of newly developed Zn-0.8%Li-(Mg, Ag) alloys for guided bone regeneration, Mater. Sci. Eng. C 99 (2019) 1021–1034.
[43] H. Baker, ASM handbook volume 3-alloy phase diagrams. US: ASM International, J. Alloys Compd. 450 (2008) 446–451.
[44] A. Drelich, P. Bowen, L. LaLonde, J. Goldman, J. Drelich, Importance of oxide film in endovascular biodegradable zinc stents, Surface Innovations 4 (2016) 1.
[45] Z. Zhang, B. Jia, H. Yang, Y. Han, Q. Wu, K. Dai, Y. Zheng, Biodegradable ZnLiCa ternary alloys for critical-sized bone defect regeneration at load-bearing sites: in vitro and in vivo studies, Bioact. Mater. 6 (11) (2021) 3999–4013.
[46] J. Young, R.G. Reddy, Synthesis, mechanical properties, and in vitro corrosion behavior of biodegradable Zn-Li-Cu alloys, J. Alloys Compd. 844 (2020) 156257.
[47] Z. Li, Z. Shi, Y. Yan, D. Zhang, K. Yang, H. Li, H. Zhang, L. Wang, Suppression mechanism of initial pitting corrosion of pure Zn by Li alloying, Corros. Sci. 189 (2021) 109564.
[48] N. Ecob, B. Ralph, The effect of grain size on deformation twinning in a textured zinc alloy, J. Mater. Sci. 18 (8) (1983) 2419–2429.
[49] T. Gancarz, J. Pstrus, G. Cempura, K. Berent, Influence of Li addition to Zn-Al alloys on Cu substrate during spreading test and after aging treatment, J. Electron. Mater. 45 (12) (2016) 6067–6078.
[50] D. Wei, L. Li, X. Min, F. Fang, Z. Xie, J. Jiang, Microstructure and mechanical properties of heavily cold drawn pearlitic steel wires: effects of low temperature annealing, Mater. Charact. 153 (2019) 108–114.
[51] J. Lan, X. Shen, J. Liu, L. Hua, Strengthening mechanisms of 2A14 aluminum alloy with cold deformation prior to artificial aging, Mater. Sci. Eng. A 745 (2019) 517–535.
[52] T. Al-Samman, Modification of texture and microstructure of magnesium alloy extrusions by particle-stimulated recrystallization, Mater. Sci. Eng. A 560 (2013) 561–566.
[53] M.S. Ardakani, E. Mostaed, M. Sikora-Jasinska, S. Kampe, J. Drelich, The effects of alloying with Cu and Mn and thermal treatments on the mechanical instability of Zn-0.05Mg alloy, Mater. Sci. Eng. A 770 (2020) 138529.
[54] P. Luo, D. McDonald, W. Xu, S. Palanisamy, M. Dargusch, K. Xia, A modified Hall–Petch relationship in ultrafine-grained titanium recycled from chips by equal channel angular pressing, Scr. Mater. 66 (10) (2012) 785–788.
[55] H. Huang, C. Chen, Z. Wang, Y. Li, G. Yuan, Effect of pretreatment and annealing on microstructure and mechanical properties of Mg-1.5Zn-0.25Gd (at%) alloys reinforced with quasicrystal, Mater. Sci. Eng. A 581 (2013) 73–82.
[56] Y. Wang, J. Huang, Texture analysis in hexagonal materials, Mater. Chem. Phys. 81 (1) (2003) 11–26.
[57] M. Watroba, W. Bednarczyk, J. Kawalko, P. Bala, Effect of zirconium microaddition on the microstructure and mechanical properties of Zn-Zr alloys, Mater. Charact. 142 (2018) 187–194.

[58] S. Zhu, C. Wu, G. Li, Y. Zheng, J. Nie, Creep properties of biodegradable Zn-0.1Li alloy at human body temperature: implications for its durability as stents, Mater. Res. Lett. 7 (9) (2019) 347–353.
[59] J. Venezuela, M. Dargusch, The influence of alloying and fabrication techniques on the mechanical properties, biodegradability and biocompatibility of zinc: a comprehensive review, Acta Biomater. 87 (2019) 1–40.
[60] D. Song, A. Ma, J. Jiang, P. Lin, D. Yang, J. Fan, Corrosion behavior of equal-channel-angular-pressed pure magnesium in NaCl aqueous solution, Corros. Sci. 52 (2) (2010) 481–490.